Direct numerical simulation and global stability analysis of three-dimensional instabilities in a lid-driven cavity

Jérèmie Chicheportiche *, Xavier Merle, Xavier Gloerfelt, Jean-Christophe Robinet

Laboratoire SINUMEF, Arts et Métiers ParisTech, 75013 Paris, France

Abstract

The first bifurcation in a lid-driven cavity characterized by three-dimensional Taylor–Görtler-Like instabilities is investigated for a cubical cavity with spanwise periodic boundary conditions at $Re = 1000$. The modes predicted by a global linear stability analysis are compared to the results of a direct numerical simulation. The amplification rate, and the shape of the three-dimensional perturbation fields from the direct numerical simulation are in very good agreement with the characteristics of the steady S1 mode from the stability analysis, showing that this mode dominates the other unstable unsteady modes. ***To cite this article: J. Chicheportiche et al., C. R. Mecanique 336 (2008).***

© 2008 Académie des sciences. Published by Elsevier Masson SAS. All rights reserved.

Résumé

Simulation numérique directe et analyse de stabilité globale des instabilités tridimensionnelles dans une cavité entraînée. Le but de cette étude est d'étudier les instabilités de type Taylor–Görtler qui mènent à la première bifurcation d'un écoulement de cavité entraînée. Les modes prédits par une analyse de stabilité linéaire globale sont comparés aux résultats d'une simulation numérique directe d'une cavité cubique à $Re = 1000$ avec des conditions aux limites périodiques dans la troisième direction. Le taux d'amplification et la forme des perturbations issues de la simulation numérique directe permettent clairement d'identifier le mode stationnaire S1 de l'analyse de stabilité, qui domine les autres instabilités instationnaires. ***Pour citer cet article : J. Chicheportiche et al., C. R. Mecanique 336 (2008).***

© 2008 Académie des sciences. Published by Elsevier Masson SAS. All rights reserved.

Keywords: Fluid mechanics; Lid-driven cavity; Global instabilities; Direct numerical simulation

Mots-clés : Mécanique des fluides ; Cavité entraînée ; Instabilités globales ; Simulation numérique directe

* Corresponding author.
E-mail addresses: jeremie.chicheportiche@paris.ensam.fr (J. Chicheportiche), xavier.merle@paris.ensam.fr (X. Merle), xavier.gloerfelt@paris.ensam.fr (X. Gloerfelt), jean-christophe.robinet@paris.ensam.fr (J.-C. Robinet).

1. Introduction

The study of instabilities in a 3D lid-driven cavity is an active field of research. The cavities often considered both numerically or experimentally have no-slip boundary conditions in the spanwise direction. For low Reynolds numbers, these endwalls induce a quick destabilization of the steady flow toward an unsteady one. Three-dimensional structures, called Taylor–Görtler-Like (TGL) vortices are identified in the experiments of Koseff and Street [1]. They are triggered by the curvature of the primary eddy formed by the motion of the upper wall. The role of endwalls is crucial as underlined by Albensoeder and Kuhlmann [2]. Since the present investigation focuses on the onset of the centrifugal instabilities, spanwise periodic conditions are used in the simulations to suppress the role of the endwalls. The conditions of the onset of TGL vortices are then investigated. Linear stability analysis can help to answer this question. The global stability theory proves to be a powerful tool to study strongly non-parallel flows as the lid-driven cavity [3]. Nevertheless the stability analysis gives only the potentially unstable modes, but cannot predict the dominant instability, or the combination of instabilities, which drives the flow at $Re = 1000$. The aim of the present study is to compare direct numerical simulations (DNS) and global linear stability approach to identify the mechanism of transition.

In the first part of the paper, the equations solved by the global stability code are described. Several unstable modes are identified for a square cavity, in accordance with the work of Theofilis et al. [3]. The numerical methods for the incompressible DNS solver are detailed in the second part. The flow in a cubical cavity at $Re = 1000$, based on the unitary length of the cavity, is validated with the benchmark of Albensoeder and Kuhlmann [4]. In the last part, a comparison between the DNS results and the stability analysis is realized, and shows which instability triggers the first bifurcation and the onset of non-linear TGL vortices.

2. Global linear stability analysis

The proposed stability analysis is based on the classical perturbation technique where the instantaneous flow $\mathbf{q} = (u, v, w, p)^t$ is the superimposition of unknown fluctuations $\hat{\mathbf{q}}$ on a given 2D steady basic flow $\bar{\mathbf{Q}}$: $\mathbf{q}(x, y, z, t) = \bar{\mathbf{Q}}(x, y) + \epsilon \hat{\mathbf{q}}(x, y, z, t)$ where $\epsilon \ll 1$ and $\hat{\mathbf{q}}(x, y, z, t) = \tilde{\mathbf{q}}(x, y) \exp(\mathrm{i}(\beta z - \omega t)) + complex\ conjugate$. The perturbation is then non-homogeneous in the x- and y-directions. Since a temporal approach is adopted, the spanwise wavenumber β is a real parameter, whereas the global circular frequency is the unknown complex number $\omega = \omega_r + \mathrm{i}\omega_i$. After introducing this decomposition in the dimensionless 3D incompressible Navier–Stokes equations, a linearization leads to the following equations:

$$\frac{1}{Re}\left(\frac{\partial^2 \tilde{u}}{\partial x^2} + \frac{\partial^2 \tilde{u}}{\partial y^2}\right) - \bar{U}\frac{\partial \tilde{u}}{\partial x} - \frac{\partial \tilde{p}}{\partial x} - \bar{V}\frac{\partial \tilde{u}}{\partial y} + \left(-\frac{\beta^2}{Re} - \frac{\partial \bar{U}}{\partial x}\right)\tilde{u} - \frac{\partial \bar{U}}{\partial y}\tilde{v} = -\mathrm{i}\omega\tilde{u}$$

$$\frac{1}{Re}\left(\frac{\partial^2 \tilde{v}}{\partial x^2} + \frac{\partial^2 \tilde{v}}{\partial y^2}\right) - \bar{U}\frac{\partial \tilde{v}}{\partial x} - \frac{\partial \tilde{p}}{\partial y} - \bar{V}\frac{\partial \tilde{v}}{\partial y} + \left(-\frac{\beta^2}{Re} - \frac{\partial \bar{V}}{\partial y}\right)\tilde{v} - \frac{\partial \bar{V}}{\partial x}\tilde{u} = -\mathrm{i}\omega\tilde{v}$$

$$\frac{1}{Re}\left(\frac{\partial^2 \tilde{w}}{\partial x^2} + \frac{\partial^2 \tilde{w}}{\partial y^2}\right) - \bar{U}\frac{\partial \tilde{w}}{\partial x} - \mathrm{i}\beta\tilde{p} - \bar{V}\frac{\partial \tilde{w}}{\partial y} - \frac{\beta^2}{Re}\tilde{w} = -\mathrm{i}\omega\tilde{w}$$

$$\frac{\partial \tilde{u}}{\partial x} + \frac{\partial \tilde{v}}{\partial y} + \mathrm{i}\beta\tilde{w} = 0$$

These equations can be written as a complex non-symmetric generalized eigenproblem, with eigenvalue ω and eigenvector $\tilde{\mathbf{q}}$: $[A(Re, \beta) - \omega B(Re, \beta)]\tilde{\mathbf{q}} = 0$. The problem is discretized on a non-uniform Cartesian grid refined near the walls. A finite difference scheme, optimized in the wavenumber space, along with a coordinate transform are used to evaluate the first and second derivatives [5]. Lastly, the eigenvalue problem is solved with an Implicitly Restarted Arnoldi Method [6]. As a result, the imaginary and real parts of ω pertain respectively to the growth/damping rate and the frequency of an instability mode. If $\omega_i < 0$ the perturbation decreases in time so the flow is stable, whereas if $\omega_i > 0$ the flow is unstable.

The basic flows for the square cavity at $Re = 1000$, obtained on two grids of 125^2 and 150^2 points with a 2D version of the incompressible solver described later, are in good agreement with the benchmark datas of Botella and Peyret [7]. The results from the two grids are used in the stability code with no interpolation, and allow to quantify the convergence of the eigenmodes. In Table 1, the characteristics of the four least-stable instability modes are given.

Table 1
Maxima of amplication rate and circular frequency of the first four eigenmodes, given for 125^2 and 150^2 point grids

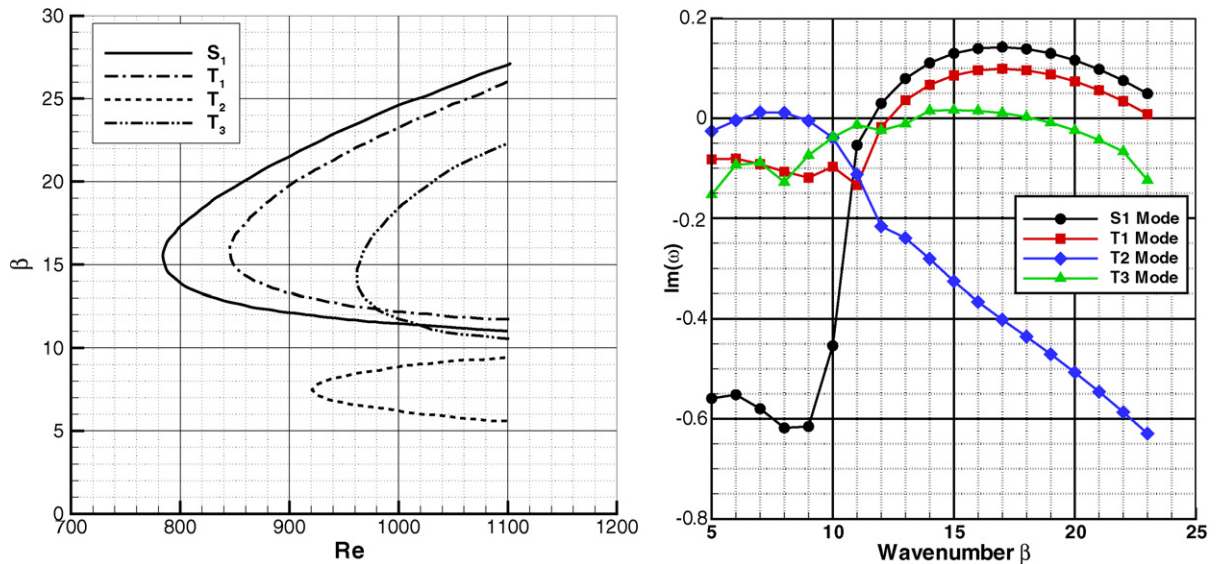| $Re = 1000$	**S1**, $\beta = 17.0$		**T1**, $\beta = 17.0$		**T2**, $\beta = 7.0$		**T3**, $\beta = 15.0$	
	ω_i	ω_r	ω_i	ω_r	ω_i	ω_r	ω_i	ω_r
125^2	0.1422	0.0000	0.0988	0.6967	0.0118	0.4962	0.0162	1.3721
150^2	0.1430	0.0000	0.0995	0.6971	0.0117	0.4966	0.0168	1.3730

Fig. 1. Neutral curves on the left, and amplification rates versus the spanwise wavenumber on the right, at $Re = 1000$ for the first four eigenmodes (grid 125^2).

They are referred to as S1 for the steady mode and T1, T2, T3 for the traveling modes, already described by Theofilis et al. [3]. The amplification rate and the frequency of each modes converge with two digits after the decimal point when the grid is refined.

The neutral curves for the four modes, depicted in Fig. 1, are in very good agreement with those of Theofilis et al. [3]. They represent the limit of stability of a mode in the parameter space (Re, β). The first critical Reynolds number $Re_c \simeq 780$, for $\beta \simeq 15$, is associated with the S1 mode. The unsteady modes T1, T2, T3 become unstable respectively for $(Re_c, \beta) \simeq (840, 15)$, $(920, 7.5)$, and $(960, 14)$. Note that the corresponding most amplified wavenumber is very close for the S1 and T1 modes, whereas the preferred wavenumber of T2 is well distinct. For $Re = 1000$, all these modes are potentially unstable, and the dependence of the amplification rate ω_i on the spanwise wavenumber is shown in Fig 1. The growth rates of T2 and T3 are very weak, so that the flow is dominated by the competitive modes S1 and T1. In their experiments for a square cavity with a spanwise aspect ratio of 3, Benson and Aidun [8] identify an unsteady flow, whose frequency is very close to the one of T1, as noted by Theofilis et al. [3]. To understand which mode is selected when the effects of endwalls are not taken into account, direct numerical simulations are now performed with periodic conditions in the spanwise direction.

3. Direct numerical simulation

The 3D incompressible Navier–Stokes equations are solved in dimensionless form. Since the velocity–pressure formulation is retained, the strategy to be adopted is either grid staggering or collocation to store working variables. Since central differencing is used, we favor the first strategy to avoid grid-to-grid oscillations. Spatial discretization of non-linear terms are performed with a compact six-order finite difference scheme with coefficients calculated for a non-uniform Cartesian staggered grid. Viscous terms are discretized with second-order accuracy in space and integrated in time with a second-order implicit Crank–Nicolson, requiring the solution of a linear algebraic system
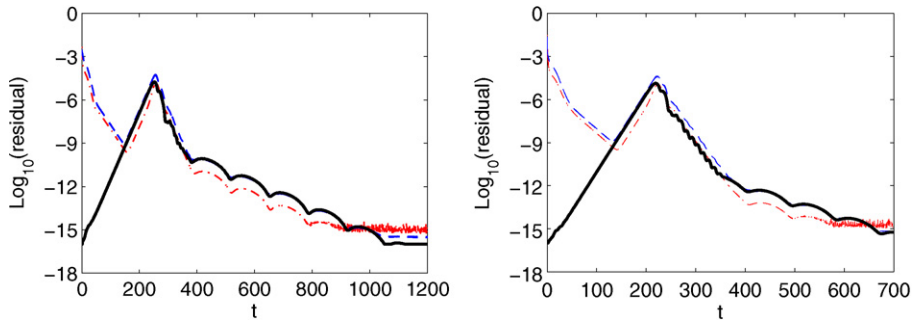
Fig. 2. Histories of residuals for the $36 \times 36 \times 26$ (left) and $64 \times 64 \times 44$ (right) point grids: u, v (- - -); w, (——); p, (- · · ·).
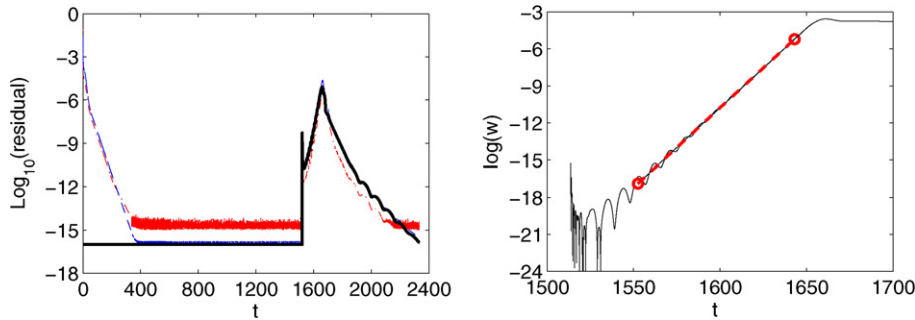

Fig. 3. Left: Histories of residuals for the $100 \times 100 \times 64$ point grid: u, v (- - -); w, (——); p, (- · · ·). Right: Logarithmic evolution of the spanwise component of flow versus time for $100 \times 100 \times 64$ grid and $a_{\mathrm{noise}} = 10^{-6}$.

with a block-tridiagonal matrix. Other terms are advanced with a third-order Adams–Bashforth scheme leading to a classical semi-implicit method. Interpolation between node and vertex grids is a crucial step performed with six-order Lagrange interpolation on a non-uniform grid. The satisfaction of discrete divergence-free velocities is enforced by a projection method ensuring second-order accuracy in time for both velocity and pressure. The spanwise boundary conditions of the cavity are periodic, thus, a spectral collocation based on a Fourier decomposition is used in the spanwise direction.

The calculations are performed for a cubical cavity at $Re = 1000$, i.e. with a spanwise extent $\Lambda = 1$, corresponding to $\beta = 2\pi$. They are started impulsively from a null field, and the evolution of the residuals, defined as $\sum_{i=1}^{N_{\mathrm{tot}}} (f(\mathbf{x}_i, t + \Delta t) - f(\mathbf{x}_i, t))/N_{\mathrm{tot}}$ (where N_{tot} is the total number of points of each grid) for the different variables $f = u, v, w, p$ are reproduced in Fig. 2 and in Fig. 3 for three refined grids. The history of the residual values in Fig. 2 are very similar for the two coarser grids. All the values seem to decrease except for the spanwise velocity residual which rises gradually from 10^{-16}. As it reaches a threshold value of 10^{-9}, the slope of the three other residuals is inverted. At the inversion time, it is verified that the intermediate state corresponds exactly to the 2D steady state previously used as an entry for the stability analysis. During the quasi-linear rise which follows, the flow becomes three-dimensional. The driving instability then saturates and a new phase of decrease of the residuals is visible, leading to a final steady non-linear three dimensional state. The scenario is a little bit different for the finer grid. The spanwise component remains zero at the beginning of the calculation, so that the other residuals decrease until zero machine is reached. The intermediate 2D flow obtained at convergence is numerically stable as seen in Fig. 3 for $400 < t < 1500$. By analogy with the destabilization mechanism observed for the coarser grids, a very small perturbation on w with an amplitude a_{noise} is introduced at $t = 1500$. The residuals are then seen to rise and fall toward the 3D steady state previously observed, and carefully validated with the benchmark of Albensoeder and Kuhlmann [4]. In particular, the wavelength of the final three dimensional structures is closed to one third of the spanwise extent (i.e. $\beta = 18.85$). The level of convergence is quantified by extracting the growth rate ω_i from the history of the spanwise component w. By plotting the logarithm of w in Fig. 3 during the development phase of the 3D instability (between $t = 1520$ and 1640 for the finer grid), a well-defined exponential growth is identified, whose slope gives ω_i. As the grid is refined,

Table 2

Left: amplification rates $\omega_{i_{DNS}}$ and wavenumber β_{DNS} for different grids and levels of noise a_{noise}. Right: values for the first four eigenmodes from the stability calculation at $\beta = 18.85$ (150^2 point grid)

	$\omega_{i_{DNS}}$	β_{DNS}
$36 \times 36 \times 26$	0.1075	17.27
$64 \times 64 \times 44$	0.1226	18.43
$100 \times 100 \times 64$, $a_{noise} = 10^{-3}$	0.1287	18.70
$100 \times 100 \times 64$, $a_{noise} = 10^{-6}$	0.1289	18.70
$150 \times 150 \times 96$, $a_{noise} = 10^{-6}$	0.1311	18.85

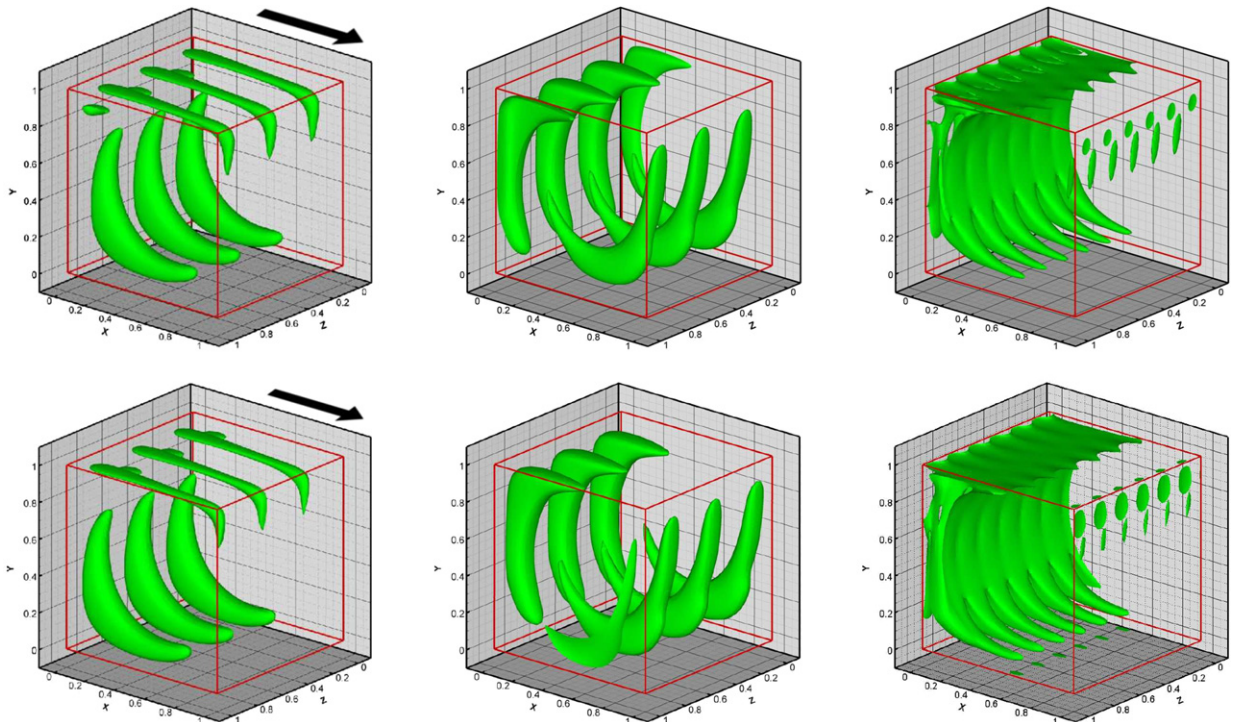| $\beta = 18.85$	ω_i
$S1$ mode	0.1322
$T1$ mode	0.0896
$T2$ mode	−0.3826
$T3$ mode	−0.0061

Fig. 4. Isocontour of perturbative field for DNS ($100 \times 100 \times 64$ points, first row), and S1 stability mode ($150 \times 150 \times 44$ points, second row): u-component of velocity (left), v-component of velocity (centre), and norm of the vorticity (right). The lid motion is indicated by the arrow.

the growth rate from DNS, in Table 2, converges toward a value which is close to the growth rate of the mode S1 for $\beta = 18.85$. The influence of the level of noise used to trigger the instability on the finer grid remains very weak.

To confirm that the final non-linear 3D structures are indeed induced by the S1 instability, the perturbation fields during the linear phase are extracted. For that purpose, the 2D basic flow is subtracted from instantaneous fields taken at one instant in the middle of the exponential growth phase previously identified ($t = 1600$). The perturbation fields obtained are compared to the S1 eigenmode from the stability analysis in Fig. 4. We observe a great similarity between these fields. Moreover, the S1 mode is clearly a centrifugal instability which is related to TGL vortices. Finally, the instability mode observed is the one having the greatest growth rate in the stability analysis, which is the S1 mode. The spanwise wavenumber is selected by the periodic conditions to be close to a multiple of the wavelength corresponding to the maximal amplification, leading to $\beta = 3 \times 2\pi/\Lambda$. This selection mechanism has been described by Albensoeder and Kuhlmann [2], by varying Λ.

4. Conclusion

In this investigation, a three-dimensional steady Taylor–Görtler-Like flow is found for a cubical lid-driven cavity at $Re = 1000$ with periodic spanwise boundary conditions. This steady mode corresponds to the S1 mode of a stability

analysis, and dominates the other unsteady unstable modes predicted by the theoretical approach. The wavelength of the vortical structures matches a submultiple of the spanwise extent of the cavity. The bifurcation reported with no-slip endwalls is quite different and can lead directly to an unsteady flow. Further investigations are needed to characterize the second bifurcation toward an unsteady flow for spanwise periodic conditions with the DNS solver.

Acknowledgements

References

[1] J.R. Koseff, R.L. Street, Visualization studies of a shear driven three-dimensional recirculating flow, ASME J. Fluids Engrg. 33 (1984) 594–602.
[2] S. Albensoeder, H.C. Kuhlmann, Nonlinear three-dimensional flow in the lid-driven square cavity, J. Fluid Mech. 569 (2006) 465–480.
[3] V. Theofilis, P.W. Duck, J. Owen, Viscous linear stability analysis of rectangular duct and cavity flows, J. Fluid Mech. 505 (2004) 249–286.
[4] S. Albensoeder, H.C. Kuhlmann, Accurate three-dimensional lid-driven cavity flow, J. Comput. Phys. 206 (2005) 536–558.
[5] X. Merle, J.-C. Robinet, A. Lerat, Efficient numerical method for global linear stability problem 37th AIAA Fluid Dynamics Conference and Exhibit, Miami, FL, 25–28 June, AIAA Paper 2007–3978, 2007.
[6] R.B. Lehoucq, D.C. Sorensen, C. Yang, ARPACK user's guide: solution of large scale eigenvalue problems with Implicity Restarted Arnoldi Methods, 1997, http://www.caam.rice.edu/software/ARPACK/.
[7] O. Botella, R. Peyret, Benchmark spectral results on the lid-driven cavity flow, Computers and Fluids 27 (1998) 421–433.
[8] J.D. Benson, C.K. Aidun, Transition to unsteady nonperiodic state in a through-flow lid-driven cavity, Phys. Fluids A 4 (10) (1992) 2316–2319.